

## FINDING THE FIRST COSMIC EXPLOSIONS I: PAIR-INSTABILITY SUPERNOVAE

DANIEL J. WHALEN<sup>1</sup>, WESLEY EVEN<sup>2</sup>, LUCILLE H. FREY<sup>2,3</sup>, JARRETT L. JOHNSON<sup>4</sup>, C. C. LOVEKIN<sup>5</sup>, CHRIS L. FRYER<sup>6</sup>, MASSIMO STIAVELLI<sup>7</sup>, DANIEL E. HOLZ<sup>8</sup>, ALEXANDER HEGER<sup>9</sup>, S. E. WOOSLEY<sup>10</sup> AND AIMEE L. HUNGERFORD<sup>2</sup>

*Draft version June 5, 2019*

### ABSTRACT

The first stars are the key to the formation of primitive galaxies, early cosmological reionization and chemical enrichment, and the origin of supermassive black holes. Unfortunately, in spite of their extreme luminosities, individual Population III stars will likely remain beyond the reach of direct observation for decades to come. However, their properties could be revealed by their supernova explosions, which may soon be detected by a new generation of NIR observatories such as *JWST* and *WFIRST*. We present light curves and spectra for Pop III pair-instability supernovae calculated with the Los Alamos radiation hydrodynamics code RAGE. Our numerical simulations account for the interaction of the blast with realistic circumstellar envelopes, the opacity of the envelope, and Lyman absorption by the neutral IGM at high redshift, all of which are crucial to computing the NIR signatures of the first cosmic explosions. We find that *JWST* will detect pair-instability supernovae out to  $z \gtrsim 30$ , *WFIRST* will detect them in all-sky surveys out to  $z \sim 15 - 20$  and *LSST* and *Pan-STARRS* will find them at  $z \lesssim 7 - 8$ . The discovery of these ancient explosions will probe the first stellar populations and reveal the existence of primitive galaxies that might not otherwise have been detected.

*Subject headings:* early universe – galaxies: high-redshift – stars: early-type – supernovae: general – radiative transfer – hydrodynamics – shocks

### 1. INTRODUCTION

Population III (Pop III) stars are the key to understanding primeval galaxies, the chemical enrichment and reionization of the early IGM, and the origin of supermassive black holes. Unfortunately, because these stars are at the edge of the universe there are no observational constraints on their masses. Even with their extreme luminosities (Schaerer 2002) and the advent of new near infrared (NIR) observatories such as the *James Webb Space Telescope* (*JWST*), the *Wide-Field Infrared Survey Telescope* (*WFIRST*) and the *Thirty-Meter Telescope* (*TMT*), individual Pop III stars will remain beyond the reach of observation for decades to come (e.g. Gardner et al. 2006, but see Rydberg et al. 2012 for the possibility of detection by strong gravitational lensing).

Numerical simulations indicate that primordial stars are born in  $10^5 - 10^6 M_{\odot}$  dark matter halos at

$z \sim 20 - 30$ . The original calculations suggested that they are  $30 - 500 M_{\odot}$  and form in isolation, one per halo (Bromm et al. 1999; Abel et al. 2000, 2002; Bromm et al. 2002; Nakamura & Umemura 2001; O’Shea & Norman 2007; Yoshida et al. 2008). Newer models have since shown that some Pop III stars form in binaries (Turk et al. 2009), and that some may form with much lower masses in small clusters of up to a dozen (Stacy et al. 2010; Clark et al. 2011; Greif et al. 2011, 2012). Nevertheless, in spite of their increasing sophistication these simulations fall well short of predicting the Pop III initial mass function (IMF) because none of them realistically bridge the gap between the formation and fragmentation of the protostellar disk and its photoevaporation up to a Myr later (Omukai & Palla 2001, 2003; Tan & McKee 2004; McKee & Tan 2008; Stacy et al. 2012; Hosokawa et al. 2011).

Some have tried to estimate the masses of Pop III stars by reconciling their nucleosynthetic yields with the chemical abundances found in ancient, dim metal-poor stars in the Galactic halo, some of which may have formed in the ashes of the first stars (Beers & Christlieb 2005; Frebel et al. 2005; Caffau et al. 2012). The current consensus is that  $15 - 40 M_{\odot}$  Pop III stars die in core-collapse supernovae (CC SNe) and  $140 - 260 M_{\odot}$  stars explode as far more energetic pair-instability supernovae (PI SNe), with 100 times the energy of Type Ia or Type II explosions (Heger & Woosley 2002). The metals expelled by the first SNe into the IGM depend on how mixing and fallback onto compact remnants occurs inside the star prior to shock breakout from its surface. Joggerst et al. (2010) (hereafter JET10) find that in  $15 - 40 M_{\odot}$  Pop III SNe the shock fully disrupts the shells of elements in the star, heavily mixing the ejecta by the time it ruptures the surface. In PI SNe the shells expand almost homol-

<sup>1</sup> McWilliams Fellow, Department of Physics, Carnegie Mellon University, Pittsburgh, PA 15213 [dwhalen@lanl.gov](mailto:dwhalen@lanl.gov)

<sup>2</sup> XTD-6, Los Alamos National Laboratory, Los Alamos, NM 87545

<sup>3</sup> Department of Computer Science, University of New Mexico, Albuquerque, NM 87131

<sup>4</sup> Director’s Fellow, T-2, Los Alamos National Laboratory, Los Alamos, NM 87545

<sup>5</sup> T-2, Los Alamos National Laboratory, Los Alamos, NM 87545

<sup>6</sup> CCS-2, Los Alamos National Laboratory, Los Alamos, NM 87545

<sup>7</sup> Space Telescope Science Institute, 3700 San Martin Drive, Baltimore, MD 21218

<sup>8</sup> Enrico Fermi Institute, Department of Physics, and Kavli Institute for Cosmological Physics, University of Chicago, Chicago, IL 60637, USA

<sup>9</sup> Monash Centre for Astrophysics, Monash University, Victoria, 3800, Australia

<sup>10</sup> Department of Astronomy and Astrophysics, UCSC, Santa Cruz, CA 95064

ogously, with only occasional minor mixing between the O and He layers prior to breakout (Joggerst & Whalen 2011) (see also Chen et al. 2011).

JET10 find that the aggregate yields of 15 - 40  $M_{\odot}$  Pop III CC SNe are consistent with the chemical abundances measured in a sample of  $\sim 130$  extremely metal-poor (EMP) stars (Cayrel et al. 2004; Lai et al. 2008), suggesting that some primordial stars may have much lower masses than inferred in the first numerical simulations. These results together with the failure to detect the odd-even nucleosynthetic pattern of PI SNe in extremely metal poor stars to date have led some to conclude that Pop III were only tens of solar masses, not hundreds, and that Pop III PI SNe may not have occurred in the early universe. However, such conclusions are premature for several reasons. First, the gas in which later generations of stars formed may have been enriched by PI SNe to metallicities above those targeted by surveys thus far (Karlsson et al. 2008) (see also Ren et al. 2012, for details on a new PI SN survey). Second, extracting the Pop III IMF from the fossil abundance record remains problematic. Larger samples of EMP stars are needed to better constrain SN yields, systematic error has been found in measurements of some elements, and how the first metals are taken up into new stars is not fully understood. The recent discovery that rotating Pop III stars down to 65  $M_{\odot}$  may die as PI SNe significantly increases the likelihood of such events at high redshift (Chatzopoulos & Wheeler 2012). Finally, and perhaps most compellingly, PI SNe have been discovered today (Gal-Yam et al. 2009) in environments that are far less favorable to the formation of massive progenitors than in the early universe (Pan et al. 2012b).

The properties of the first stars may soon be unveiled by their SN explosions, which could be found by *JWST* or *WFIRST* because they are thousands of times brighter than their progenitors or their host galaxies. Past studies have considered detection thresholds for PI SNe for various instruments at  $z \sim 5$  (Scannapieco et al. 2005),  $6 < z < 15$  (Pan et al. 2012a), and in rough terms out to  $z \sim 30$  (Hummel et al. 2012). However, to accurately model the NIR signatures of these events, PI SNe must be simulated with radiation hydrodynamics in realistic circumstellar envelopes and their spectra must be convolved with Lyman absorption by the neutral IGM at early epochs and redshifted. The interaction of the SN with the envelope shrouding the star and the opacity of the envelope itself both crucially shape the spectra in the source frame and govern how much flux is eventually redshifted into the NIR. Lyman absorption by neutral hydrogen prior to the era of reionization determines how much flux from these ancient SNe is removed or scattered from our line of sight. Previous studies, including earlier calculations of PI SN light curves and spectra (Kasen et al. 2011), did not incorporate these effects.

Accounting for these processes, Whalen et al. (2012b) recently found that *JWST* will detect PI SNe out to  $z \sim 30$  and *WFIRST* will detect them out to  $z \sim 15 - 20$ . However, their grid of models did not cover the full range of stellar structures expected for 140 - 260  $M_{\odot}$  Pop III stars. We have now calculated the NIR signals of Pop III PI SNe for both blue compact and red hypergiant progenitors from  $7 < z < 30$  with the Los Alamos RAGE and SPECTRUM codes. In §2 we review the PI explosion

mechanism, the physics that governs the presupernova structure of the star, and our Kepler Pop III PI progenitor and SN models. We describe how these explosions are evolved in RAGE and post processed in SPECTRUM to obtain source frame light curves and spectra in §3 and we examine blast profiles and spectra in §4. In §5 we present NIR light curves for Pop III PI SNe in the observer frame and determine their detection limits as a function of redshift. In §6 we calculate PI SN detection rates for  $5 < z < 30$ , and in §7 we conclude.

## 2. PI SN MODELS

PI SNe were first proposed by Rakavy & Shaviv (1967) and Barkat et al. (1967) and have been studied numerous times since (see Heger & Woosley 2002, and references therein). Pop III stars above 100  $M_{\odot}$  encounter the pair instability after central carbon burning, when thermal energy creates  $e^+e^-$  pairs rather than maintaining pressure support against collapse. The cores of these stars subsequently contract, triggering explosive thermonuclear burning of O and Si. Above 140  $M_{\odot}$ , the energy that is released completely unbinds the star, and no black hole is formed. At 260  $M_{\odot}$  the core of the star reaches temperatures that are high enough for alpha particles to be photo-disintegrated into free nucleons, which consumes as much energy per unit mass as was released by all preceding burning. The star collapses instead of exploding. PI SNe are the most energetic thermonuclear events in the universe, with yields of up to  $10^{53}$  erg for 260  $M_{\odot}$  stars.

The early spectral signatures of Pop III PI SNe heavily depend on the radius and structure of the star in addition to the explosion energy, the interaction of the blast with the envelope, the opacity of the envelope, and absorption by the IGM. Shock temperatures at breakout are lower for large stars than for compact stars of equal mass because the shock has expanded to a greater radius and done more work on its environment. Early spectra from the explosions of compact blue stars are therefore harder than those of red giants. The structure of the star determines the degree to which its interior is mixed before the shock breaks out from its surface and hence the lines that appear in its spectra. The size and structure of the progenitor in turn are governed by its metallicity and by internal convection over its life.

### 2.1. Semi-Convective Mixing

Convection can determine if a very massive Pop III star dies as a compact blue giant or a red hypergiant. As described in detail in Scannapieco et al. (2005), the convection zone of the star can approach, touch or even penetrate the lower hydrogen layers, mixing them with carbon dredged up from the core from He burning. When these two high temperature components mix, they burn violently, boosting energy production rates in the H shell by up to several orders of magnitude. This, together with the now greater opacity of the lower hydrogen layer, can puff up the star by more than an order of magnitude in radius.

### 2.2. Metallicity

Gas in high-redshift halos that is enriched to metallicities below  $10^{-3.5} Z_{\odot}$  fragments on mass scales that are

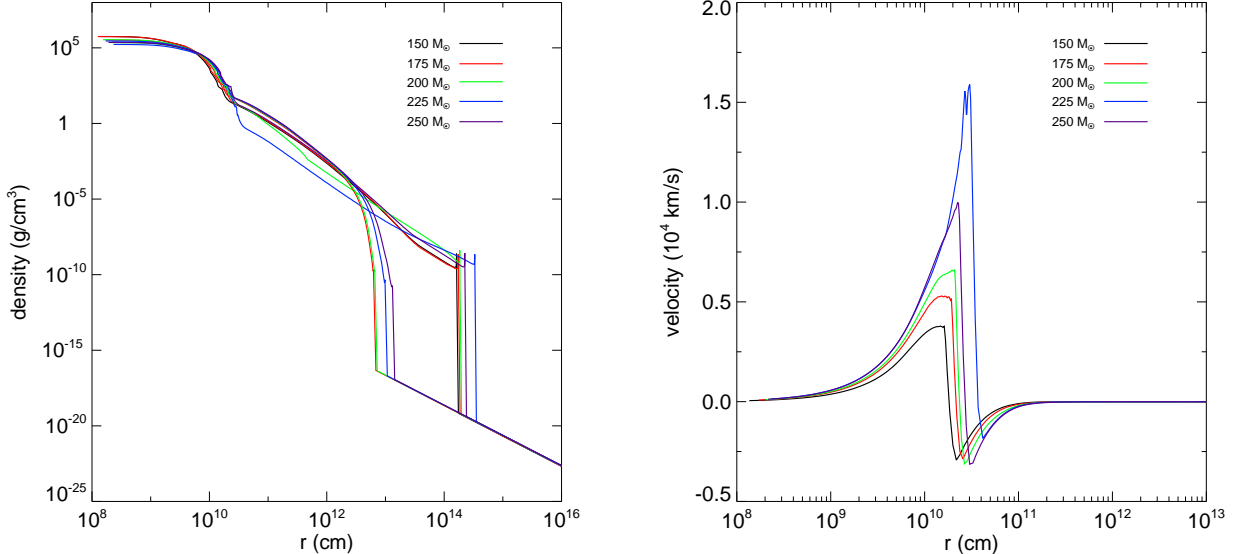


FIG. 1.— Kepler PI SN explosion and stellar envelope profiles. Left panel: densities for all nine models. The surface of each star is marked by the abrupt drop in density by ten orders of magnitude at  $r \sim 10^{13}$  cm in the four z-series profiles and a few  $\times 10^{14}$  cm in the five u-series stars. A wind with a total mass of  $0.1 M_{\odot}$ , a velocity of  $10^8$  cm/s, and a free-streaming  $r^{-2}$  profile is extended from the surface of the star out to the uniform relic H II region surrounding the star, which is not visible on this plot. Right panel: velocity profiles for the u-series stars. Both the outgoing shock and ongoing collapse of the outer layers of the star are visible.

essentially identical to those of pristine gas and forms very massive stars (e.g. Bromm et al. 2001; Mackey et al. 2003; Smith & Sigurdsson 2007). However, these small metallicities are more than enough to enhance CNO reaction and energy generation rates in the hydrogen burning layers of the star, inflating the stellar envelope as much as convection. Since there is a strong degeneracy between the effects of metals and convection on the structure of the star, the full range of light curves and spectra for Pop III PI SNe can be as easily spanned by metallicity as convective overshoot, as we demonstrate below.

### 2.3. Explosive Mixing

Mixing within the star during the explosion can determine which elements appear in emission lines over time. In the frame of the shock, the photosphere from which photons escape descends into the ejecta over time as each fluid element expands and the ejecta is diluted. If Rayleigh-Taylor (RT) mixing precedes shock breakout, it can dredge heavy elements up from a deeper mass coordinate to the photosphere and expose them to the IGM at much earlier times. Since mixing is minimal in Pop III PI SNe, the absence of Fe or Ni lines soon after shock breakout would be one of several markers of the event. The evidence or absence of mixing in early spectra is one manner in which a rudimentary IMF could begin to be built up by detections of Pop III explosions.

### 2.4. Kepler

To capture the structure of the progenitor, we evolve 150, 175, 200, 225, and 250  $M_{\odot}$  zero-metallicity stars (z-series) and  $10^{-4} Z_{\odot}$  stars (u-series) from the zero age main sequence to the onset of collapse in the 1D Lagrangian stellar evolution code Kepler (Weaver et al. 1978; Woosley et al. 2002). The SN begins when this collapse triggers explosive O and Si burning. Unlike the CC SN simulations of JET10, in which the blast must

be artificially launched with a piston and the explosion energy is a free parameter, the PI SN is an emergent feature of our stellar evolution model, and its energy is set by how much O and Si burns. The blast was followed until the end of all nuclear burning at  $\sim 20$  s, when the shock was still deep inside the star. We calculate energy generation with a 19-isotope network up to the point of oxygen depletion in the core and with a 128-isotope quasi-equilibrium network thereafter. The z-series 150  $M_{\odot}$  star collapses to a black hole without an explosion. The number of mass zones on the grid ranged from 1000 - 1200 and was always sufficient to resolve all salient structures of the star and SN. We show density and velocity profiles for our explosions in Figure 1 and summarize our grid of models in Table 1. As in all previous studies of PI SNe, we consider only non-rotating progenitors.

We use metallicity rather than convective overshoot to parametrize the structures of our progenitors because for any given star the size of the central convection zone is uncertain but  $Z = 0$  and  $10^{-4} Z_{\odot}$  bracket the metallicities over which 140 - 260  $M_{\odot}$  Pop III stars are thought to form (Mackey et al. 2003; Smith & Sigurdsson 2007; Smith et al. 2009). As we show in Figure 1, these two metallicities yield compact blue giant and red hypergiant envelopes similar to those obtained by varying semi-convective mixing in Scannapieco et al. (2005). All u-series stars in our study die as red hypergiants and all z-series stars die as compact blue giants. The light curves and spectra for our SNe should therefore bracket those that will be found in observations. However, we note that most 140 - 260  $M_{\odot}$  Pop III stars are expected to exhibit convective mixing and die as red stars rather than blue stars.

## 3. RAGE AND SPECTRUM SIMULATIONS

We propagate the shock through the interior of the star, its surface, and then out into the surrounding

TABLE 1  
KEPLER PI SN MODELS (MASSES ARE IN  $M_{\odot}$ )

model	$M_{He}$	$R$ ( $10^{13}$ cm)	$E$ ( $10^{51}$ erg)	$M_{Ni}$
u150	72	16.2	9.0	0.07
u175	84.4	17.4	21.3	0.70
u200	96.7	18.4	33	5.09
u225	103.5	33.3	46.7	16.5
u250	124	22.5	69.2	37.9
z175	84.3	0.62	14.6	0
z200	96.9	0.66	27.8	1.9
z225	110.1	0.98	42.5	8.73
z250	123.5	1.31	63.2	23.1

medium with the radiation hydrodynamics code RAGE (Gittings et al. 2008). RAGE (Radiation Adaptive Grid Eulerian) is a multidimensional adaptive mesh refinement (AMR) radiation hydrodynamics code developed at Los Alamos National Laboratory (LANL). RAGE couples second-order conservative Godunov hydrodynamics to grey or multigroup flux-limited diffusion (FLD) to model strongly radiating flows. RAGE utilizes the extensive LANL OPLIB database of atomic opacities<sup>11</sup> (Magee et al. 1995) and can also evolve multimaterial flows with a variety of equations of state (EOS). We describe the physics implemented in our RAGE models and why it is needed to capture the features of our light curves in detail in Frey et al. (2012) (hereafter FET12): multispecies advection, grey FLD radiation transport with 2-temperature (2T) physics, energy deposition from radioactive decay of  $^{56}\text{Ni}$ , and no self-gravity. In particular, 2T radiation transport, in which radiation and matter temperatures are evolved separately, better models shock breakout and its aftermath when matter and radiation can be out of equilibrium. This is an important improvement over earlier 1T models of PI SN explosions. We evolve mass fractions for 15 elements, the even numbered elements predominantly synthesized in PI SNe.

### 3.1. Initial Grid

We map densities, velocities, specific internal energies ( $\text{erg gm}^{-1}$ ), and species mass fractions for the explosion and star from Kepler together with a circumstellar envelope onto a 50,000 zone 1D spherical AMR mesh in RAGE. Since radiation energy densities were not explicitly evolved in the Kepler models, we initialize them in RAGE as

$$E_{rad} = aT^4, \quad (1)$$

where  $a = 7.564 \times 10^{-15} \text{ erg cm}^{-3} \text{ K}^{-4}$  is the radiation constant and  $T$  is the gas temperature. Also, because the gas energy in Kepler includes contributions by ionization states of atoms, we unambiguously construct the specific internal energy from  $T$  with

$$E_{gas} = C_V T, \quad (2)$$

where  $C_V = 7.919 \times 10^7 \text{ erg K}^{-1}$  is the specific heat of the gas. Because there is little mixing in the star as the shock propagates to the surface, the radial distribution of elements in the star is essentially frozen in mass coordinate at death and expands homologously into

space thereafter. One-dimensional simulations are therefore sufficient to capture all key attributes of our PI SN light curves and spectra.

At the beginning of the simulation we allocate 5000 zones from the center of the grid to the edge of the shock in the velocity profile on the root grid. We permit up to five levels of refinement in both the initial interpolation of the profiles onto this grid and throughout the simulation. This guarantees that all important density and velocity features in the initial blast profile are resolved by at least 10 zones on the root grid and can be subsampled by up to 32 times more zones as needed. It also ensures that the photosphere of the shock is always fully resolved, since failure to do so can lead to underestimates of luminosity during post processing. The shock radii in our Kepler profiles vary from  $1.5 - 3.0 \times 10^{10}$  cm and our initial root grid has a resolution of  $1.0 \times 10^8$  cm, with an outer boundary at  $5.0 \times 10^{12}$  cm.

We impose reflecting and outflow boundary conditions on the fluid and radiation flows at the inner and outer boundaries of the mesh, respectively. When the calculation is begun, Courant times are initially small due to high temperatures, large velocities and small cell sizes. To reduce execution times and to accommodate the expansion of the ejecta, we periodically regrid the profiles onto a larger mesh as the explosion grows, as described in detail in FET12. Each time we regrid the blast we allocate 5000 zones out to either the edge of the shock (pre-breakout) or to the edge of the radiation front (post-breakout – we take the point at which the radiation temperature falls below a few tenths of an eV to be the edge of the front). The inner boundary is always 0 cm and the outer boundary of the final, largest mesh in our models is  $1.0 \times 10^{18}$  cm. Evolving the explosion out to 3 yr requires about 30 days on 32 processors on LANL platforms.

### 3.2. Circumstellar Winds

Just as there are no observational constraints on Pop III stars, there are none on their ambient environments either. Numerical simulations of I-front breakout from primordial halos show that Pop III stars usually drive all the baryons from their halos in supersonic ionized flows and die in low-density H II regions (Whalen et al. 2004; Kitayama et al. 2004; Alvarez et al. 2006; Abel et al. 2007; Wise & Abel 2008a). These relic H II regions have relatively flat density profiles  $n \sim 0.1 - 1 \text{ cm}^{-3}$  out to 100 - 200 pc. Pop III stars are not thought to lose much mass over their lifetimes because there are no metals in their atmospheres to drive strong winds (Kudritzki 2000; Baraffe et al. 2001; Vink et al. 2001; Krtečka & Kubát 2006). However, we allow for the possibility that they had some winds for several reasons. First, mass loss from very massive stars is usually just parametrized by metallicity, not calculated from first principles with radiation hydrodynamics and other physics (e.g., Meynet et al. 1994). Extrapolating zero wind from no metallicity could miss mass loss by other means, such as helium opacity in extreme luminosities, hydromagnetic flows, or pulsational ejections (Heger & Woosley 2002). Second, mixing in rotating Pop III stars, which we do not consider here, can dredge metals up from the interior of the star to its surface and drive winds later in its life (e.g., Ekström et al. 2008),

<sup>11</sup> <http://aphysics2/www.t4.lanl.gov/cgi-bin/opacity/tops.pl>

although the mass loss is found to be minor. Finally, there are no observations to rule out winds from zero-metallicity stars. We therefore extend a low-mass wind profile from the surface of the star out to the relic H II region:

$$\rho_W(r) = \frac{\dot{m}}{4\pi r^2 v_W}, \quad (3)$$

where  $\dot{m}$  is the mass loss rate due to the wind and  $v_W$  is the wind speed. The mass loss rate is

$$\dot{m} = \frac{M_{tot}}{t_{MSL}}, \quad (4)$$

where  $M_{tot}$  and  $t_{MSL}$  are the total mass loss and main sequence lifetime of the star, respectively. We take  $M_{tot} = 0.1 M_\odot$ ,  $v_w = 1000 \text{ km s}^{-1}$ , H and He mass fractions to be 76% and 24%, and  $T = 0.01 \text{ eV}$  in all our models. The radius at which the density of the wind is smoothly joined to the H II region, whose density we take to be  $0.1 \text{ cm}^{-3}$ , varies with the radius of each star, but is typically  $10^{17} - 10^{18} \text{ cm}$ . Density and velocity profiles for the wind are shown in Figure 1 (where the sharp drop in density at the edge of the star where breakout occurs is also evident). If the wind density falls to the H II region density before the edge of the grid it is smoothly joined to that density at that radius.

### 3.3. Ionization of the Wind

To determine if the progenitor ionizes the wind we use the ZEUS-MP code to model the outgoing ionization front from the surface of the star (Whalen & Norman 2006, 2008a,b). We center a blue  $175 M_\odot$  z-series star and its wind on a 1D spherical mesh with 200 zones and inner and outer boundaries at  $7.0 \times 10^{12} \text{ cm}$  and  $1.0 \times 10^{15} \text{ cm}$ , the surface of the star and the outer regions of the wind. To enhance grid resolution in the densest regions of the wind we use logarithmically ratioed zones where

$$\frac{\Delta r_{i+1}}{\Delta r_i} = 1.043. \quad (5)$$

We propagate of the I-front from the star into the wind with multifrequency UV transport, with 40 bins uniformly partitioned in energy from 0.255 - 13.6 eV and 80 logarithmically spaced bins from 13.6 - 90 eV. We take the spectrum of the star to be blackbody, normalized to ionizing photon emission rates, surface temperatures, and luminosities from Schaerer (2002).

We find that the blue star easily ionizes the wind on timescales of  $\sim 10^4 \text{ yr}$ . The gas temperature is 40,000 K near the surface of the star, where rapid ionizations and recombinations in the large fluxes and densities there lead to greater heating than at  $10^{15} \text{ cm}$ , where temperatures are  $\sim 25,000 \text{ K}$ . Because the least massive blue star in our study easily ionizes the wind and has the highest surface wind density, we conclude that the winds around all z-series progenitors in our simulations are ionized.

Red u-series progenitors have surface temperatures that are too low to emit ionizing UV but still ionize their wind envelopes because they are blue for most of their lives. They become too cool to sustain ionizing flux only in their final few hundred kyr. Recombination times in

the wind therefore determine its ionization state when the star dies, without the need for a transport calculation:

$$t_{rec} = \frac{1}{n_e \alpha(T)}. \quad (6)$$

Here,  $n_e$  is the electron number density and  $\alpha(T)$  is the recombination rate coefficient for hydrogen, which we take to be  $2.59 \times 10^{-13} T_4^{-0.75} \text{ s}^{-1}$ , where  $T_4$  is the temperature in units of  $10^4 \text{ K}$ . With the ionized gas temperatures we found for the compact  $175 M_\odot$  star and the densities of the modest winds in our study, recombination times vary from 5 - 50 kyr in the vicinity of the star, ensuring that the wind is neutral when the star explodes. For simplicity, we take the wind to be neutral around all the stars in our study, so our luminosities at shock breakout for z-series stars will be lower limits because neutral envelopes allow less flux to escape until they are fully ionized by the breakout pulse. We note that the ionized wind itself has significant luminosity due to recombinations (Rydberg et al. 2010), but we are primarily interested in the transient flux from the explosion, not emission from its envelope.

### 3.4. SPECTRUM

To calculate a spectrum from a RAGE profile, we map its densities, temperatures, velocities and mass fractions onto a new grid in the LANL SPECTRUM code. SPECTRUM performs a direct sum of the luminosity of every fluid element in this discretized snapshot to compute the total flux that exits the ejecta along the line of sight at every wavelength. This procedure is described in detail in FET12, and is formulated to account for Doppler shifts and time dilation due to the relativistic expansion of the ejecta. We also calculate the intensities of emission lines and the attenuation of flux along the line of sight with detailed LANL OPLIB opacities, thereby capturing both limb darkening and the absorption lines imprinted on the flux by intervening material in the ejecta and wind.

As explained in FET12, gas densities, velocities, mass fractions and radiation temperatures from the finest levels of refinement of the RAGE AMR grid are first extracted and ordered by radius into separate files, one variable per file. These profiles typically contain more than 50,000 radial zones, and constraints on machine memory and time prevent us from using all of them to calculate spectra, so only a subset of the points is mapped onto the SPECTRUM grid. We first sample the RAGE radiation energy density profile inward from the outer boundary to find the position of the radiation front, which we take to be where  $aT^4$  rises above  $1.0 \text{ erg/cm}^3$ . We then find the radius of the  $\tau = 20$  surface by integrating the optical depth due to Thomson scattering inward from the outer boundary ( $\kappa_{Th} = 0.288$  for H and He gas at primordial composition). This yields the greatest depth in the ejecta from which photons can escape because  $\kappa_{Th}$  is the minimum opacity the photons would encounter.

The extracted gas densities, velocities, temperatures and species mass fractions from RAGE are then interpolated onto a 2D grid in  $r$  and  $\theta$  in SPECTRUM whose inner and outer boundaries are 0 and  $10^{18} \text{ cm}$ , respectively. One hundred uniform zones in log radius are allocated from the center of the grid to the  $\tau = 20$  surface.

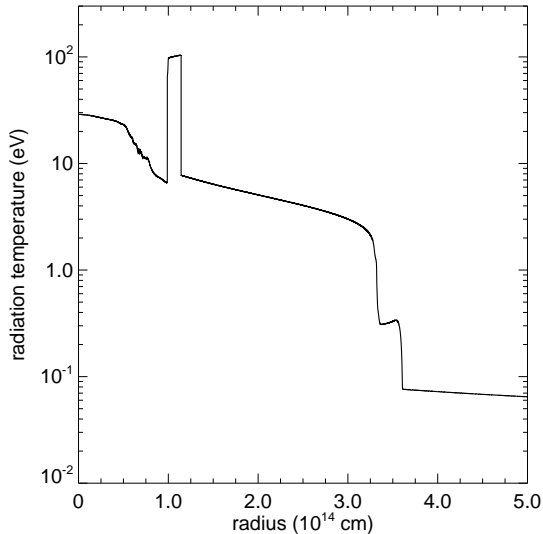


FIG. 2.— The highly radiative shock in the u225 model at  $7.26 \times 10^4$  s. The shock is at  $1.2 \times 10^{14}$  cm, deep inside the star. Photons from the shock cannot reach the surface of the star from this depth because of Thomson scattering in its upper layers. The 0.3 eV plateau in the temperature at the stellar surface at  $3.2 \times 10^{14}$  cm is optical radiation from the star propagating out into the wind before shock breakout.

The region between the  $\tau = 20$  surface and the edge of the radiation front is partitioned into 5000 uniform zones in radius. The wind between the front and the outer boundary of the grid is then divided into 100 uniform zones in log radius, for a total of 5200 radial bins. The data in each of these new radial bins is mass-averaged to ensure that the SPECTRUM grid captures very sharp features from the original RAGE profile. The grid is uniformly discretized into 160 bins in  $\mu = \cos\theta$  from -1 to 1. Our choice of mesh yielded good convergence in spectrum tests, fully resolving regions of the flow from which photons can escape the ejecta and only lightly sampling those from which they cannot.

Summing the luminosities at each wavelength in one spectrum yields the bolometric luminosity of the SN at that moment. Many such luminosities computed over a range of times constitutes the light curve of the explosion. We sample shock breakout with 50 spectra uniformly spaced in time and the rest of the light curve with another 200 spectra logarithmically distributed in time out to 3 yr. One SPECTRUM calculation averages 3 - 6 hours on 32 processors on LANL machines.

#### 4. PI SN BLAST PROFILES, LIGHT CURVES AND SPECTRA

The onset of explosive burning drives a strongly radiating shock from the O layer into the upper layers of the star, as we show in Figure 2. At this point the shock is not visible to an external observer because its photons are trapped by  $e^-$  scattering in the intervening layers, so they are simply advected outward by the fluid flow.

##### 4.1. Shock Breakout

When the shock reaches the surface of the star it abruptly accelerates to large velocities in the steep density gradient there, as we show in the left panel of Figure 3. The acceleration heats the shock, and it releases

an intense burst of photons upon being exposed to the low density IGM, as shown in the right panel of Figure 3. The advancing radiation front is visible as the plateau in gas temperature at 50 eV and  $1.2 \times 10^{13}$  cm at 3990 s and 30 eV and  $2.0 \times 10^{13}$  cm at 4550 s. The plateau temperatures are those to which the radiation front heats the ambient wind as it passes through it; the temperature of the shock that is emitting the radiation itself is much higher, as we show below. The temperature of the plateau falls as the shock expands, cools and its spectrum softens. Note that there are serious departures from self-similarity in the velocity profiles at late stages of breakout (third plot in the left panel of Figure 3) because of significant coupling between radiation and gas in the shock. This is one reason Sedov-Taylor profiles are not good solutions for shock breakout (Fryer et al. 2010) and why radiation transport is required to model the flow.

We show bolometric luminosities for the breakout transient for the u-series and z-series PI SNe in the left and right panels of Figure 4, respectively. For comparison, we show the luminosity of the shock for the u225 explosion if it is assumed to be a blackbody,

$$L = 4\pi r^2 \sigma T^4, \quad (7)$$

where  $\sigma$  is the Stefan-Boltzmann constant and the temperature  $T$  of the shock is taken at the  $\tau_{Th} = 1$  surface, where  $\kappa_{Th} = 0.288$ . If photons of all energies broke through the surface of the star at the same time, the duration of the initial transient would be comparable to the light crossing time of the star, since photons emitted from its poles and its equator would reach an observer at times that differ by the time it takes light to cross the star. Given that u-series stars have radii of a few  $10^{14}$  cm, their breakout transients would last 1 - 2 hr, which is consistent with the width of the  $4\pi r^2 \sigma T^4$  approximation to the luminosity of the pulse. In reality, the transient is smeared out over longer times because photons at different energies escape the shock from a range of optical depths over time and because radiation remains strongly coupled to the shock past breakout (as shown in the third velocity profile in Figure 3). The resulting pulse is dimmer but longer. The width of the transient is much greater for giant red u-series stars because of their larger radii, lower surface densities, and thus broader regions from which photons break free of the shock.

We show spectra for the breakout pulse for u250 and z250 PI SNe in the left and right panels of Figure 5, respectively. The z250 transient is mostly x-rays and the u250 pulse is both x-rays and hard UV. The spectrum of the u250 transient is softer because the progenitor is much larger, and the shock has done more  $PdV$  work on its surroundings and cooled more by the time it breaks out of the star. The ionization of the surrounding wind envelope is particularly evident in the z250 breakout spectra, in which prominent absorption features from 100 to  $10^4$  Å in the first profile are mostly absent in the second. By the end of shock breakout the surrounding wind is completely ionized by the radiation pulse and the spectrum of the shock has essentially a blackbody profile. The absorption features are more prominent in the z250 spectra because of the higher wind densities at the

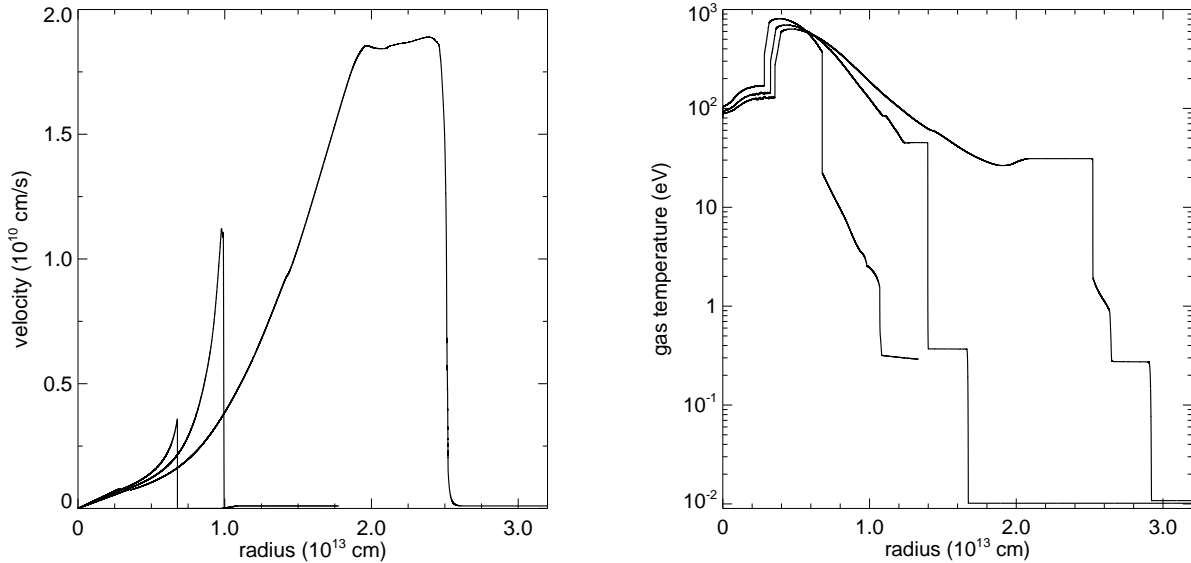


FIG. 3.— Shock breakout in the z225 explosion. Left panel: velocities, from left to right, at 3560 s, 4140 s, and 4550 s. Shock breakout through the surface of the star is evident in the abrupt jump in velocity in the second profile, and the continued acceleration of the shock down the  $r^{-2}$  density profile of the wind is visible in the third profile. Right panel: gas temperatures at 3560 s, 3990 s, and 4550 s from left to right. The radiation breakout pulse is the flat 50 eV plateau in gas temperature at  $1.2 \times 10^{13}$  cm at 4140 s. As the shock expands and cools the spectrum of the breakout pulse softens, which is why the gas temperature in its wake has fallen to  $\sim 30$  eV at 4550 s.

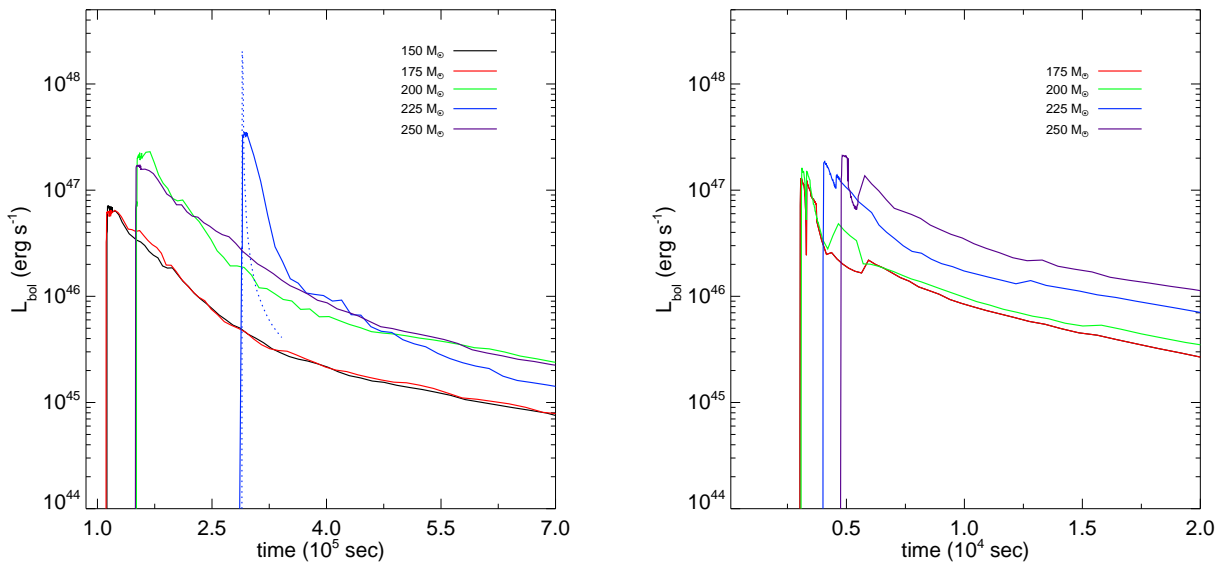


FIG. 4.— Bolometric luminosities Left panel: u-series PI SNe. Right panel: z-series PI SNe.

surface of this smaller star.

Peak bolometric luminosities vary from  $7 \times 10^{46}$  to  $4 \times 10^{47}$  erg/s, or  $\sim 2500$  times the luminosity of our galaxy. There is a general trend of greater luminosity with explosion energy and later breakout times with progenitor mass, since stellar radii increase with mass. Although the shock has a much smaller radius at breakout in the z-series than in the u-series, it has approximately the same total luminosity because it is hotter. This can be seen from how the luminosity  $L$  of a blackbody scales with radius and temperature in equation 7. Typical shock temperatures at the  $\tau = 1$  surface at breakout are  $\sim 1200$  eV in the z-series stars and  $\sim 150$  eV in the u-series stars, which roughly compensates for the factor of 10 in

radius between the two progenitors. However, we note that the shock is not a blackbody and that its luminosity is roughly an order of magnitude below that predicted by equation 7, as we show in Figure 4<sup>12</sup>. Treating SN shocks as blackbodies in general can lead to overestimates in luminosity of an order of magnitude or more at breakout, as discussed in Fryer et al. (2010).

We also note that our transport solutions yield peak bolometric luminosities that are an order of magnitude higher than those of Kasen et al. (2011). There may be

<sup>12</sup> Because of  $e^-$  scattering in the photosphere of the ejecta, the shock is more like a greybody whose luminosity  $L = 4\pi\epsilon r^2\sigma T^4$ , where  $\epsilon < 1$  is the correction to the blackbody luminosity due to scattering.

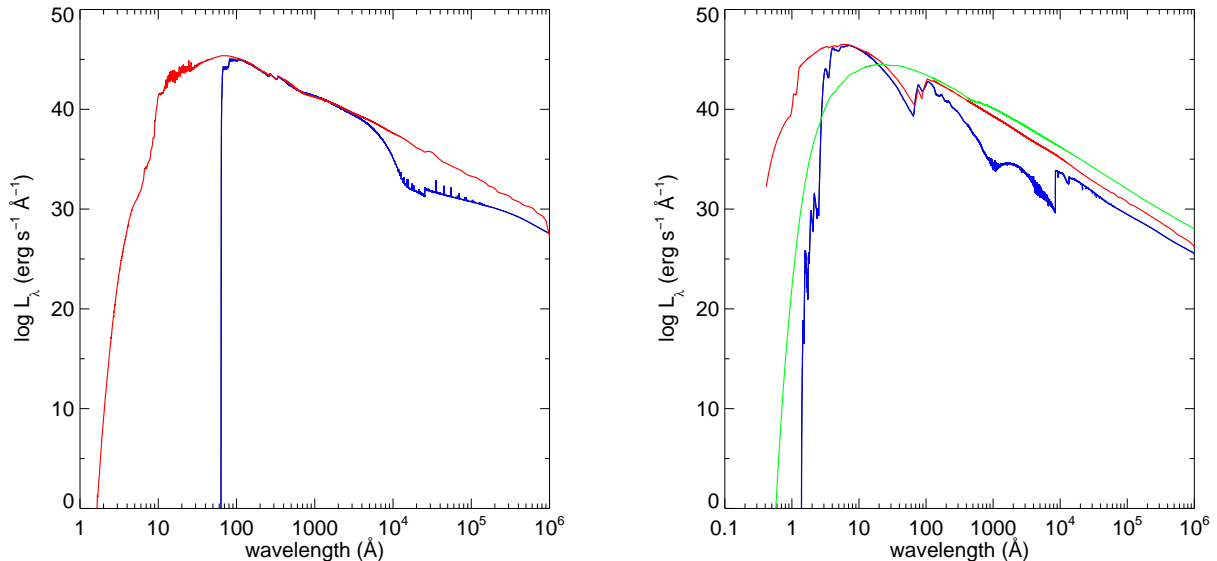


FIG. 5.— Spectra of the breakout transient. Left panel: u250 explosion. Blue:  $1.500 \times 10^5$  s; red:  $1.512 \times 10^5$  s. Right panel: z250 explosion. Blue: 4780 s; red: 4939 s; green:  $1.618 \times 10^4$  s.

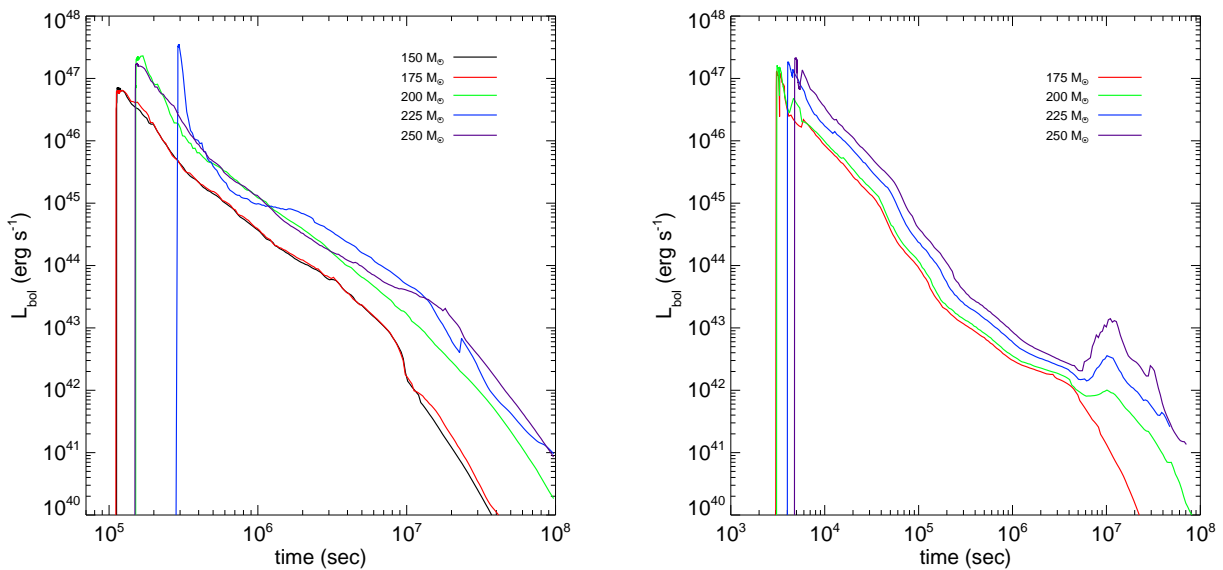


FIG. 6.— Source frame bolometric luminosities for all 9 PI SNe out to 3 yr. Left panel: u-series. Right panel: z-series. The general trend of higher luminosity with progenitor mass in each series is evident, as is the fact that u-series explosions are brighter than z-series SNe of equal progenitor mass. The resurgence in luminosity at  $\sim 10^7$  s in most of the SNe coincides with the descent of the photosphere of the shock into the hot  $^{50}\text{Ni}$  layer of the ejecta.

several reasons for this: first, we envelop the star in a wind profile which is raised to extremely high temperatures when the shock crashes through the surface of the star. This collision may account for some of the higher breakout luminosity, since there is no circumstellar shroud in the Kasen et al. (2011) simulations. Second, we use 2T radiation transport instead of 1T transport, and when radiation and matter are no longer forced to be in thermal equilibrium more photons may be emitted by the flow. We also use LANL OPLIB opacities instead of the Lawrence Livermore OPAL opacities (Iglesias & Rogers 1996; Rogers et al. 1996)<sup>13</sup> in the

Kasen et al. models, and this may too account for some of the disparity in peak luminosities. Shock breakout has been the subject of numerous analytical studies (Colgate 1974; Matzner & McKee 1999; Nakar & Sari 2010; Piro et al. 2010; Katz et al. 2012) and numerical studies (Ensmann & Burrows 1992; Blinnikov et al. 2000; Tominaga et al. 2009; Tolstov 2010; Kasen et al. 2011) in the past thirty years. One aspect of shock breakout that is unique to our study is that it is redshifted from 1 - 2 hr in duration at  $z \sim 20$  to a day or more in the observer frame.

<sup>13</sup> <http://rdc.llnl.gov>



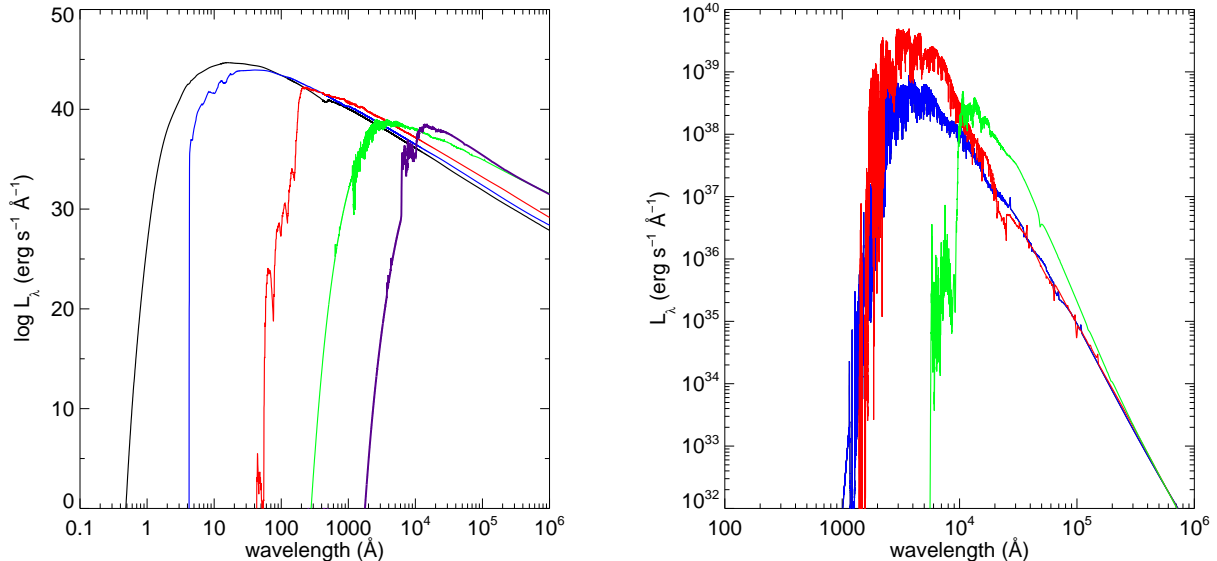


FIG. 7.— Spectral evolution of the z250 PI SN. Left panel: fireball spectra at  $1.47 \times 10^4$  s (black),  $2.77 \times 10^4$  s (blue),  $1.15 \times 10^5$  s (red),  $6.12 \times 10^6$  s (green), and  $2.30 \times 10^7$  s (purple). Right panel: spectra at  $6.12 \times 10^6$  s (blue),  $1.10 \times 10^7$  s (red) and  $2.08 \times 10^7$  s (green), the onset, peak and decline of the bump in bolometric luminosity at  $\sim 4$  months. Note the multiple P Cygni profiles of prominent lines (dips in flux blueward of the line and peaks in flux redward of the line), such as those at  $\sim 2.5 \times 10^4$  Å,  $4.0 \times 10^4$  Å,  $6.5 \times 10^4$  Å, and  $10^5$  Å at  $1.1 \times 10^7$  s.

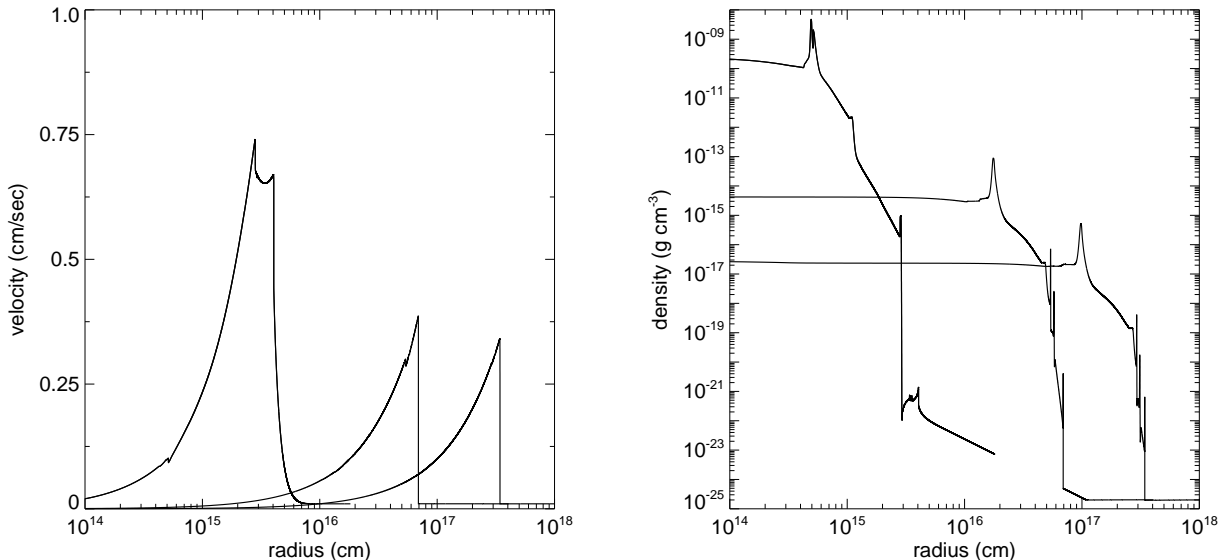


FIG. 8.— Intermediate to late-time hydrodynamical evolution of the u250 PI SN. Left panel: velocities at  $5.02 \times 10^5$  s,  $1.80 \times 10^7$  s, and  $1.0 \times 10^8$  s (left to right). Right panel: density profiles at the same times from left to right.

We show bolometric light curves out to three years for the u-series and z-series SNe in the left and right panels of Figure 6, respectively. PI SN luminosities are powered at early times by the conversion of kinetic energy into thermal energy by the shock, so they are far brighter than Type Ia and II SNe at this stage because they have much higher explosion energies. At later times their luminosity comes mostly from radioactive decay, and they are much brighter than other SNe because they synthesize more  $^{56}\text{Ni}$ : up to  $50 M_{\odot}$  compared to  $0.4 - 0.8 M_{\odot}$  and  $< 0.3 M_{\odot}$  in Type Ia and Type II SNe, respectively. They are brighter for longer times (3 years instead of 3 -

6 months for Type Ia and II SNe) because radiation diffusion timescales in their more massive ejecta are much longer:

$$t_d \sim \kappa^{\frac{1}{2}} M_{ej}^{\frac{3}{4}} E^{-\frac{3}{4}}. \quad (8)$$

Here,  $\kappa$  is the average opacity of the ejecta,  $M_{ej}$  is the mass of the ejecta, and  $E$  is the explosion energy. The luminosity generally rises with progenitor mass within each series because the explosion energy and  $^{56}\text{Ni}$  mass increase with stellar mass in both red and blue stars. All five u-series explosions exhibit a slower, more protracted decay in luminosity out to 4 months than the z-series SNe

and are more than an order of magnitude brighter over this interval. These profiles are consistent with those of Type II-p SNe, whose progenitors are also thought to be red giants with extended envelopes. Their greater luminosities over this interval are mostly due to the fact that u-series explosions create more  $^{56}\text{Ni}$  than z-series SNe for progenitors of equal mass (see Table 1).

Except for z175, there is prominent bump in all the z-series luminosities at about 4 months that lasts for about a year. As we discuss in greater detail below, this re-brightening occurs when the photosphere of the shock uncovers the hot  $^{56}\text{Ni}$  layer deep in the ejecta and its photons escape into the IGM. The magnitude and duration of the bump is proportional to the  $^{56}\text{Ni}$  mass, which explains its absence in z175 because it creates only a tenth of the  $^{56}\text{Ni}$  formed in the z200 SN. This feature is also present in the u-series explosions but at first glance does not seem to be as prominent as in the z-series. Closer scrutiny reveals that it is several times brighter than in a z-series SN of equal mass, and that it is not as prominent because the luminosity before and after the bump are higher. The peaks are higher in the u-series SNe partly because they form more  $^{56}\text{Ni}$  and partly because the photosphere extends deeper into the  $^{56}\text{Ni}$  layer upon reaching it, where gas temperatures are higher. The radii of these layers are roughly the same when the photosphere reaches them in u-series and z-series explosions of equal mass.

We show the evolution of the spectra for the z250 PI SN from shock breakout to 2 yr in the left panel of Figure 7. Two physical processes govern the evolution of the spectrum over time. First, as the fireball expands it cools, and its spectral cutoff advances to longer wavelengths over time. Second, the wind envelope that was ionized by the breakout pulse begins to recombine and absorb photons at the high energy end of the spectrum, as evidenced by the flux that is blanketed by lines at the short-wavelength limit of the spectrum. At later times flux at longer wavelengths slowly rises due to the expansion of the surface area of the photosphere. Over the wavelength scale of this plot the many thousands of lines captured by the LANL OPLIB opacities in our SPECTRUM calculation are blended together in the prominent jagged spectral features throughout the spectrum. Given how line blanketing by both the ejecta and the wind shear off the spectrum at short wavelengths, it is clear that the common practice of fitting blackbodies to light curves to approximate spectra overestimates flux at high energies from which many photons are eventually redshifted into the NIR in the observer frame.

In the right panel of Figure 7 we show spectra at the beginning, peak and decline of the bump in bolometric luminosity at  $\sim 10^7$  s for the z250 PI SN. At  $1.10 \times 10^7$  s, the emission peaks at  $\sim 1000$  Å and our SPECTRUM calculation reveals the  $\tau = 1$  surface for this wavelength to be at the outer edge of the  $^{56}\text{Ni}$  layer in the ejecta, as described above. We also note that these spectra manifest multiple P Cygni profiles for prominent lines, such as those at  $\sim 2.5 \times 10^4$  Å,  $4.0 \times 10^4$  Å,  $6.5 \times 10^4$  Å, and  $10^5$  Å at  $1.1 \times 10^7$  s. They are characterized by the absorption of flux blueward of the line and the enhancement of flux redward of the line. This occurs when line emission from a fluid parcel receding along the line of sight

from the observer is redshifted while line emission from a fluid parcel approaching the observer is blueshifted and absorbed en route to the observer. The presence of these features in our spectra validates our treatment of relativistic time dilation and Doppler shifts in SPECTRUM. While we have singled out the z250 explosion for detailed spectral analysis, all the PI SNe spectra exhibit similar features and evolution.

We plot velocity and density profiles at  $5.02 \times 10^5$  s,  $1.80 \times 10^7$  s, and  $1.0 \times 10^8$  s for the u250 explosion in the left and right panels of Figure 8. Both forward and reverse shocks are visible in the velocity profiles until nearly the end of the simulation, after which the profiles become essentially self-similar. The reverse shock forms because the forward shock must propagate through an extended red hypergiant envelope before exiting the star, and it persists until well after shock breakout. Rayleigh-Taylor instabilities can arise in the reverse shock and lead to minor to moderate mixing in such stars, as shown by Joggerst & Whalen (2011) and Chen et al. (2011). Reverse shocks also form in z-series SNe but they are not as strong because the stars are more compact and they have less time to develop before breakout. Their hydrodynamical profiles become self-similar at earlier times.

## 5. POP III PI SN DETECTION THRESHOLDS

We have calculated NIR light curves for our PI SNe with the synthetic photometry code described in Su et al. (2011). Each spectrum is redshifted to the desired value before removing the flux absorbed by intervening neutral hydrogen along the line of sight according to the prescription of Madau (1995). We then dim the spectrum by the required cosmological factors. A variety of instrument filters can be easily accommodated by our code, which linearly interpolates the least sampled data between the input spectrum and filter curve to match the other. It has additional capabilities such as reddening by dust that are not used here.

### 5.1. NIR Light Curves

At  $z \gtrsim 7$ , Lyman absorption by the neutral IGM will absorb most flux at wavelengths longer than 1216 Å. However, in principle the fireball could be brighter slightly blueward of the Lyman limit rather than redward, even with IGM absorption (see Figure 3 in Whalen et al. 2012b). At every redshift for each explosion, we calculate the NIR signal in *JWST* NIRCcam filters above and below the Lyman limit to find the filter in which the SN is brightest. We find that for all the redshifts and PI SNe in our study the explosion is most luminous just redward of 1216 Å in the source frame. We show light curves for our PI SNe at  $z = 10, 15, 20$  and 30 in Figures 9 and 10. At each redshift, light curves are plotted only for the filter in which the SN will be brightest. The detection limit in all four filters is AB magnitude 32. All five u-series explosions are visible for over 1000 days, even at  $z = 30$ . The z-series SNe are dimmer but are all still visible out to  $z = 30$  for 100 - 300 days. They have lower bolometric and NIR luminosities (and dim sooner) because they create less  $^{56}\text{Ni}$  than do the u-series. None of the light curves reach the detection threshold for 50 days, or  $\sim 1.5$  days in the source frame at  $z = 30$ , so shock breakout cannot be seen from Earth.

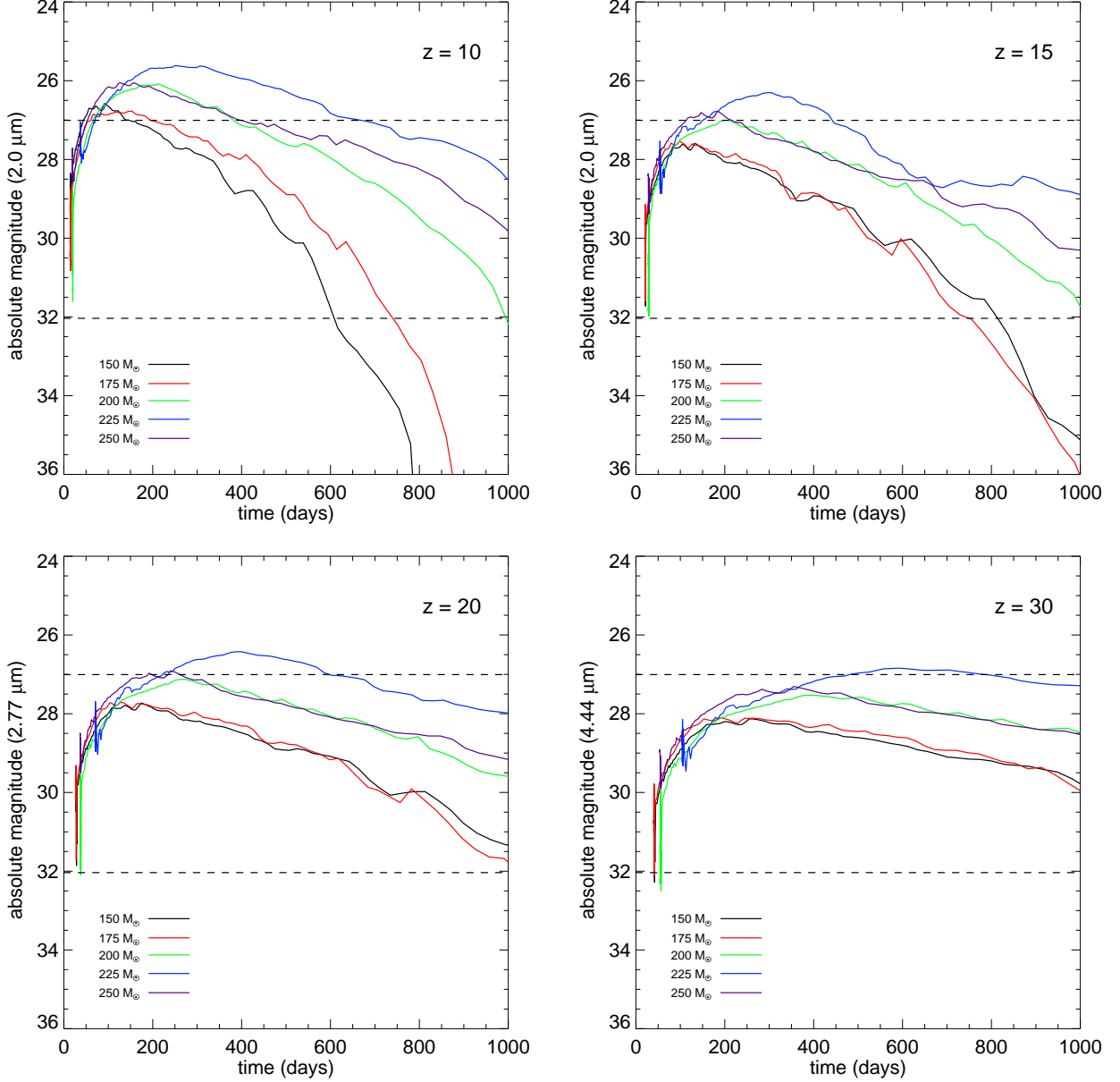


FIG. 9.— *JWST* NIRCcam light curves for the 5 u-series PI SNe. Redshifts ( $z = 10, 15, 20, 30$ ) are noted in the upper right corner of each panel. The wavelength of the optimum *JWST* filter at each redshift is noted on the y-axis labels and the times on the x-axes are in the observer frame. The dashed horizontal lines at AB mag 32 and 27 are *JWST* and *WFIRST* detection limits, respectively.

The X-rays and hard UV in the breakout transient are absorbed by the neutral IGM.

As noted earlier, as the fireball expands and cools its spectral peak steadily advances to longer wavelengths. This is manifest in the signal in the five NIR channels in Figure 11. The signal peaks at later times at longer wavelengths as the temperature of the fireball falls with time. The luminosity persists for longer times at larger wavelengths because the shock emits at these energies for a larger fraction of its cooling time than at higher energies. The expansion and cooling of the explosion, together with cosmological redshifting, also accounts for the shift of the NIR peak to later times and longer filter wavelengths with redshift in Figures 9 and 10. For example, at  $z = 10$  the u-series light curves peak from 100

- 300 days, and at  $z = 30$  they peak from 200 - 600 days. As expected, the peak magnitude of each explosion rises with redshift. The *JWST* NIR photometry limit is magnitude 31 - 32 and magnitude 29 - 30 for spectrometry. All five u-series PI SNe will be bright enough for spectroscopy out to  $z = 30$  but it will only be possible out to  $z \sim 10$  for all four z-series explosions. This is important because resolving the order in which lines appear in spectra over time could provide a powerful probe of how heavy elements are mixed in the ejecta and thus of the explosion engine itself.

As noted in Whalen et al. (2012b), the NIR flux evolves on timescales of  $\sim 1000$  days in the u-series and exhibits much more variability than the bolometric flux in the observer frame (which evolves over 40 - 90 yr) be-

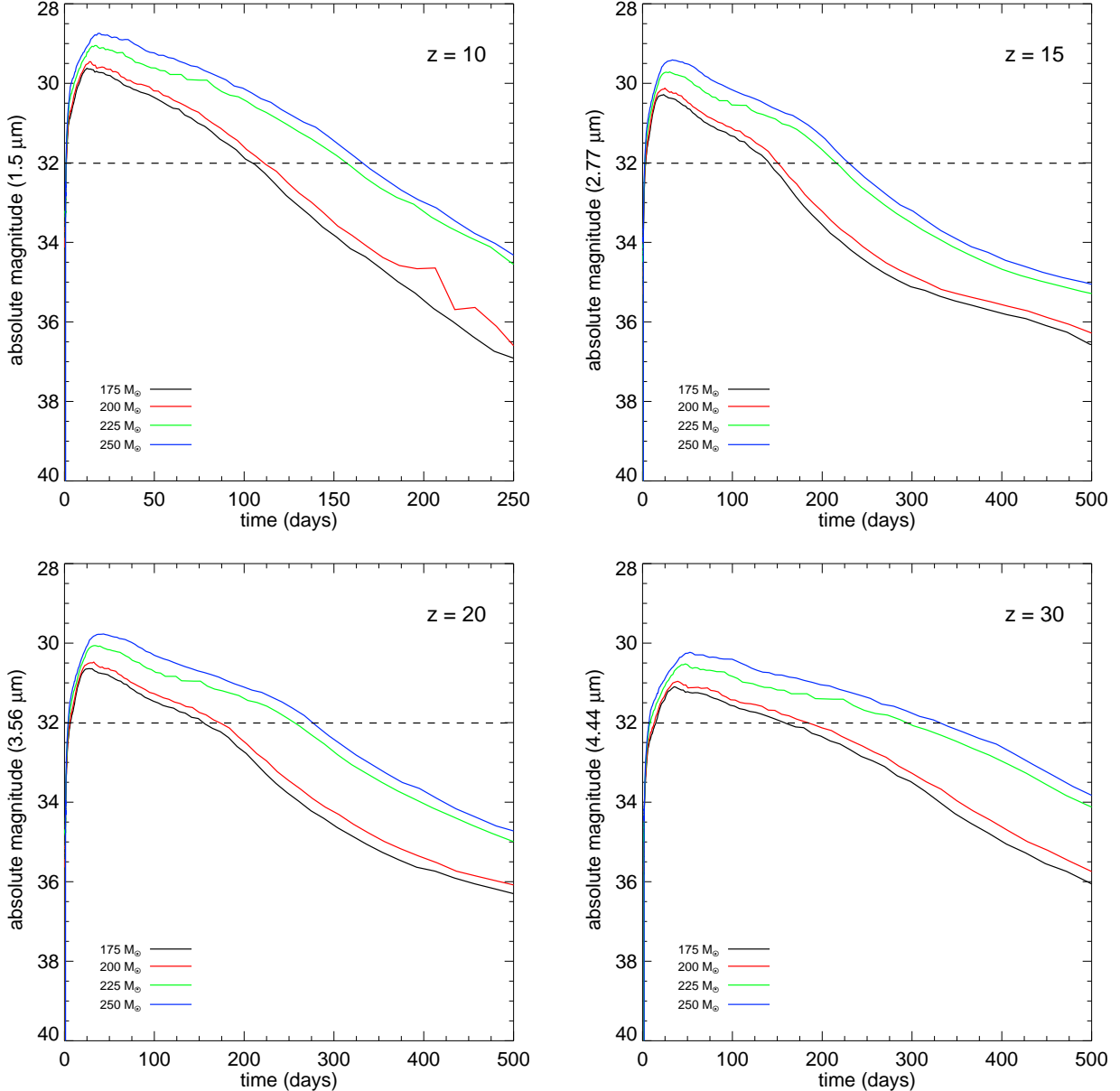


FIG. 10.— NIRCcam light curves for the 4  $z$ -series PI SNe.

cause of the expansion and cooling of the fireball. Such variability is the key to discriminating these events from primitive galaxies, with which they otherwise overlap in color-color space. Their NIR flux rises much more quickly than it falls, so it is easiest to detect them in their earliest stages but they exhibit enough variation over survey times of 1 – 5 yr to be identified at later stages as well. If Pop III PI SNe are found in the NIR, they will be thousands of times brighter than the halo or primitive galaxy that hosts them. Indeed, if a  $z \sim 15$  object exhibited any variation in luminosity in a survey, in all likelihood it would be a SN in a primeval galaxy.

### 5.2. *WFIRST*, *Euclid* & *WISH*

Pop III PI SNe could be found in large numbers in future all-sky NIR surveys such as *Euclid*, the *Wide-field Imaging Surveyor for High-Redshift* (*WISH*) and

*WFIRST*, whose target sensitivities at  $2 \mu\text{m}$  are AB magnitudes 24, 27, and 27, respectively. In Figure 9 it is clear that *WFIRST* and *WISH* will detect u-series explosions out to  $z \sim 15 - 20$ . Our calculations indicate that even at  $z = 7$ , all nine PI SNe will be above magnitude 25, so *Euclid* will only detect them below this redshift (although higher  $z$  might be possible with spectrum stacking). It may be that the optimal redshift range for locating Pop III PI SNe is  $z \sim 15 - 20$  because of Lyman-Werner (LW) UV radiative feedback. LW backgrounds from the first stars are thought to destroy  $\text{H}_2$  molecules and suppress cooling in primordial halos, causing them to grow more massive before their interiors can self-shield from LW photons, form  $\text{H}_2$  and host primordial star formation. Detailed numerical simulations show that the larger virial temperatures at the centers of such halos elevate cooling rates per  $\text{H}_2$  molecule there by 2 orders of mag-

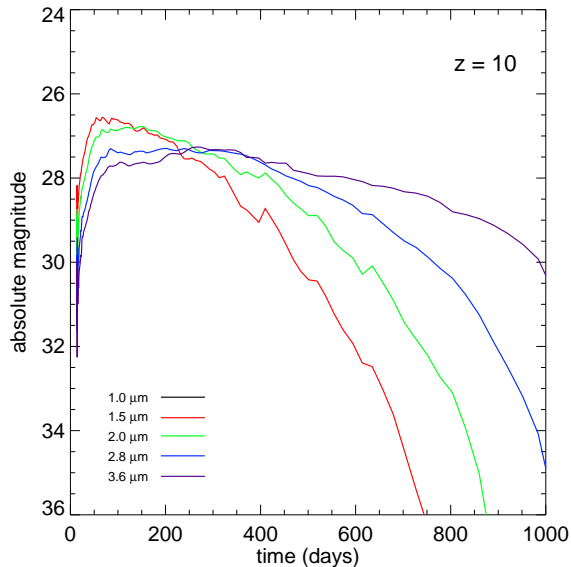


FIG. 11.— Spectral evolution of the u175 fireball in the NIR at  $z = 10$ .

nitude, leading to higher central collapse rates that favor the formation of very massive stars (O’Shea & Norman 2007; Wise & Abel 2008b). LW backgrounds sufficient to postpone Pop III star formation likely did not arise until  $z \sim 20$ , delaying baryon cooling and collapse in halos until  $z \sim 15 - 20$ . Global feedback may therefore enhance Pop III PI SNe rates at slightly lower redshifts that are well within the range of *WFIRST* and *WISH*.

### 5.3. *LSST/Pan-STARRS*

Could high- $z$  PI SNe be detected in all-sky optical and NIR surveys by the *Large Synoptic Survey Telescope (LSST)* or the *Panoramic Survey Telescope & Rapid Response System (Pan-STARRS)*? Unfortunately, above  $z \sim 10$  any source frame wavelength that could be redshifted into the optical is extinguished by Lyman absorption, but *LSST* has a target sensitivity of AB magnitude 22 in the Y band ( $0.95 - 1.070 \mu\text{m}$ ) (which could be extended to 25 with spectrum stacking) and *Pan-STARRS* has a detection limit of AB magnitude 26 in the Y band. As we show in Figure 12, all five u-series explosions will be visible to *Pan-STARRS* and marginally detectable by *LSST* at  $z = 7$ . As we discuss in greater detail below, it has been speculated that very massive Pop III stars could form down to  $z \sim 6$  in pockets of metal-free gas; if so, they could be found by these two observatories.

## 6. POP III PI SN DETECTION RATES

Although *JWST* will clearly be sensitive enough to detect  $z \gtrsim 30$  PI SNe, will it encounter such explosions over reasonable survey times given its narrow field of view? Their detection in a given survey critically depends on their event rates, which in turn are governed by primordial star formation rates (SFRs) and the Pop III IMF. Many physical processes regulate the Pop III SFR over cosmic time. Metals and UV feedback from early generations of stars are especially important, since Pop III stars can only form in pristine gas and LW photons can destroy the  $\text{H}_2$  required for baryons in halos to cool and collapse

into stars (e.g., Haiman et al. 1997; Glover & Brand 2001; Machacek et al. 2001; O’Shea & Norman 2008).

### 6.1. Semi-Analytical Estimates

The original estimates of Pop III PI SN rates were based on simple halo mass distributions and cosmological parameters that lead to first star formation at earlier epochs than do more improved parameters today (e.g., Komatsu et al. 2011). They predict event rates that range from  $0.1 - 1.5 \text{ sq. deg}^{-1} \text{ yr}^{-1}$  at  $z \sim 25$  (Wise & Abel 2005) to  $0.2$  and  $4 \text{ sq. deg}^{-1} \text{ yr}^{-1}$  at  $z \sim 25$  and  $15$ , respectively (Weinmann & Lilly 2005). These rates exclude clustering and radiative and mechanical feedback between halos (e.g., Mesinger et al. 2006; MacIntyre et al. 2006; Whalen et al. 2008a, 2010) but do consider global LW UV backgrounds that can delay star formation to slightly later epochs.

### 6.2. Numerical Simulations

Cosmological simulations that incorporate chemical and radiative feedback in varying degrees of detail have produced more realistic Pop III SFRs for the first billion years of cosmic evolution (e.g., Tornatore et al. 2007; Trenti et al. 2009; Greif et al. 2010; Maio et al. 2011; Hummel et al. 2012; Johnson et al. 2012; Wise et al. 2012). They basically agree on event rates at high redshifts but differ somewhat from the original analytical estimates, mostly because they use more recent cosmological parameters. By modeling the rise of LW backgrounds and taking a simple approach to early metal enrichment, Hummel et al. (2012) find a cumulative rate of  $\sim 0.5 - 5 \text{ sq. deg}^{-1} \text{ yr}^{-1}$  for Pop III PI SNe at  $z \gtrsim 5$ . Johnson et al. (2012) find PI SN rates of  $\sim 0.3 \text{ sq. deg}^{-1} \text{ yr}^{-1}$  over the same redshift range, which are slightly lower because their models employ more sophisticated prescriptions for chemical and mechanical feedback by SNe and assume a less top-heavy Pop III IMF. They adopted a PI SN progenitor mass range of  $140 - 260 M_\odot$  (e.g., Heger & Woosley 2002), but new models have since extended this range down to  $\sim 65 M_\odot$  (Chatzopoulos & Wheeler 2012). This new lower limit revises the PI SN rate in Johnson et al. (2012) upward by a factor of a few because of their choice of a Salpeter-like slope for the IMF.

### 6.3. $z = 15 - 20$ and $\gtrsim 25$

The cumulative PI SN rates reported by Hummel et al. (2012) imply  $10^{-3} - 10^{-2}$  events per yr per *JWST* NIR-Cam field of view ( $10 \text{ arcmin}^2$ ). Thus, *JWST* should be able to find 5 - 10 PI SNe over the lifetime of the mission, but greater numbers may be found if more time is dedicated to the surveys. We note that Lyman absorption above  $z \sim 6$ , which we include in our study, may slightly reduce the detection rates predicted by Hummel et al. (2012). All-sky surveys will find far greater numbers of PI SNe, albeit at somewhat lower redshifts. Given the PI SN rates reported by Hummel et al. (2012) and Johnson et al. (2012), up to  $\sim 10^3$  PI SNe per year could be found at  $15 < z < 20$  by *WFIRST* and *WISH*.

### 6.4. $z \lesssim 10$

As noted earlier, PI SNe may also be found in all-sky optical and NIR surveys by *LSST* or *Pan-STARRS* but

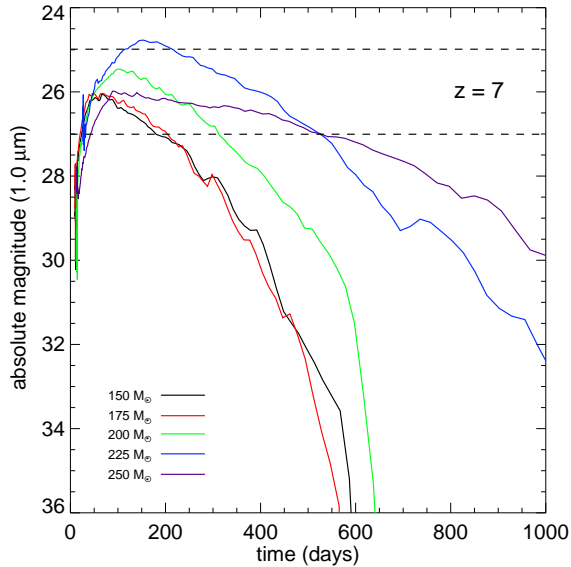


FIG. 12.— Y-band ( $1.0 \mu\text{m}$ ) light curves for all 5 u-series PI SNe at  $z = 7$ . The z-series explosions are too dim to be detected by *LSST* or *Pan-STARRS* at this redshift. The dashed horizontal lines at AB mag 27 and 25 are *Pan-STARRS* and *LSST* Y-band detection limits, respectively (these thresholds assume spectral stacking).

at lower redshifts ( $z \lesssim 10$ ) because of extinction by Lyman absorption (see also Frost et al. 2009, for a recent PI SN detection campaign in *Spitzer* data). Thus, if very massive Pop III stars form at  $6 \lesssim z \lesssim 10$ , these surveys may discover their SNe if their rates are sufficiently high. Several recent numerical simulations suggest that such stars could form in isolated pockets of metal-free gas at  $z \lesssim 6$  (Tornatore et al. 2007; Trenti & Stiavelli 2009; Trenti et al. 2009), and such environments have now been discovered at even lower redshifts Fumagalli et al. (2011). Including LW backgrounds and a simple prescription for metal enrichment based on a numerical simulation, Trenti et al. (2009) estimate a cumulative Pop III PI SN rate of  $\sim 10^{-2} \text{ yr}^{-1} \text{ deg}^{-2}$  at  $5 \lesssim z \lesssim 10$ , which implies an all-sky rate of up to  $\sim 10^3 \text{ yr}^{-1}$ .

Other cosmological simulations that include chemical enrichment and mechanical feedback by SNe have found lower Pop III SFRs (e.g., Tornatore et al. 2007; Maio et al. 2011) that imply PI SN rates that are smaller than Trenti et al. (2009). However, newer models with better treatments of LW feedback and chemical enrichment now suggest that PI SN rates in this redshift range are higher by roughly an order of magnitude than those of Tornatore et al. (2007) and Maio et al. (2011) (Hummel et al. 2012; Johnson et al. 2012). Since the Pop III SFR down to  $z \sim 7$  reported by Wise et al. (2012) is in good agreement with that found by Johnson et al. (2012), their results are also consistent with a high PI SN rate.<sup>14</sup> Overall, the results of numerical simulations indicate that the all-sky Pop III PI SN rate at  $6 \lesssim z \lesssim 10$  may lie between  $\sim 10^3 - 10^4 \text{ yr}^{-1}$ , which bodes well for their detection by *LSST* and *Pan-STARRS*.

<sup>14</sup> See also Ahn et al. (2012), who find a similar evolution of the LW background due to massive Pop III stars at high- $z$ .

## 7. CONCLUSION

We find that Pop III PI SNe will be visible in deep field surveys by *JWST* out to  $z \gtrsim 30$  and in all-sky surveys by *WFIRST* out to  $z \sim 15 - 20$ . They occur at rates that are sufficient to appear in deep field searches but will be discovered in much greater numbers in all-sky surveys that can be followed up by *JWST* and ground-based instruments. It may also be possible to find PI SNe at lower redshifts in current surveys, for example as Lyman break dropouts in the *Hubble Space Telescope* (*HST*) *CANDELS* survey or with the new *Subaru Hyper Suprime Cam*. Such strategies will be the focus of future studies.

Our calculations emphasize the detection of Pop III PI SNe in the first few years of the explosion, but could their remnants be detected at later times by different means? Whalen et al. (2008b) found that PI SNe in ionized halos eventually emit up to half of the original energy of the explosion as H and He lines as the remnant sweeps up and shocks the relic H II region. Unfortunately, the luminosity of these lines is too low and redshifted to be directly detected. However, PI SNe can also deposit up to half of their energy into CMB photons by inverse Compton scattering, and could impose excess power on the CMB at small scales (Oh et al. 2003; Kitayama & Yoshida 2005; Whalen et al. 2008b). The resolution of current ground-based CMB telescopes such as the *Atacama Cosmology Telescope* and *South Pole Telescope* approaches that required to directly image Sunyaev-Zeldovich (SZ) fluctuations from individual Pop III PI SN remnants, so future observatories may detect them.

The extreme NIR luminosities of primordial PI SNe could contribute to a NIR background excess, as has been suggested for Pop III stars themselves (i.e. Kashlinsky et al. 2005). X-rays from gas plowed up by PI SN remnants, together with radiation from early black holes, would also build up an x-ray background at high redshifts. Indeed, Johnson & Khochfar (2011) have determined that x-rays from Pop III SN remnants may have accounted for  $\sim 10\%$  of the reionizing photon budget at early times. New calculations show that PI SNe will probably not appear at 21 cm because of their lower event rates at high redshift and because their remnants will not emit enough synchrotron radiation to be directly detected by existing or future 21 cm observatories (Meiksin & Whalen 2012). The imprint of Pop III PI SNe on the CMB and NIR backgrounds will be addressed in future studies.

If, as some numerical simulations and stellar archaeology suggest, gas in primordial halos fragmented into multiple Pop III stars that were tens of solar masses instead of hundreds, then CC SNe also occurred in the primeval universe. Such explosions would be similar in brightness to those in the local universe today because their central engines mostly depend on the structure of the inner  $3 - 4 M_{\odot}$  of the star, which does not vary strongly with metallicity (Chieffi & Limongi 2004; Woosley & Heger 2007; Whalen & Fryer 2012). Because they are 100 times dimmer than PI SNe and have softer spectra, it is not clear how much of their luminosity will survive Lyman absorption by the neutral IGM at high redshift. However, because a dozen or more such stars may form in the halo, CC SNe may be more plenti-

ful than PI SNe, which would enhance their likelihood of detection. Furthermore, if the star ejects a massive shell before exploding, the SN ejecta will light up the shell in the UV upon crashing into it (superluminous Type IIn SNe – Smith & McCray 2007; van Marle et al. 2010). Such events can have luminosities that can rival those of PI SNe, and they might be visible at higher redshifts than Type II explosions (Moriya et al. 2010; Tanaka et al. 2012; Moriya et al. 2012). We are now calculating light curves and spectra for 15 - 40  $M_{\odot}$  Pop III Type II and Type IIn SNe (Whalen et al. 2012c,a).

Finally, strong gravitational lensing by massive intervening galaxies and clusters at  $z \sim 0 - 1$  could boost flux from Pop III SNe, more than compensating for Lyman absorption and improving prospects for their detection (Rydberg et al. 2012). The probability that flux from a Pop III SN would be lensed in an all-sky survey and the degree of magnification both depend on the event rate at the given redshift, and may be fairly low. We have performed preliminary calculations that place the likelihood of lensing of  $z \sim 20$  objects at  $\sim 1 - 5\%$  for flux boosts of 2 - 5. Much higher boosts (10 - 300) are possible near the edges of massive clusters but with much smaller search volumes and lower probabilities of encountering high- $z$  SNe. We continue to develop and refine Markov Chain Monte Carlo ray-tracing models of strong gravitational lensing of  $z \sim 20$  events, the highest redshifts ever attempted, in order to assess its potential to reveal primeval SNe and galaxies. Although strong lensing is not necessary for detecting PI SNe it may be key to finding CC SNe in protogalaxies prior to reionization, less of whose flux survives Lyman absorption but whose higher event rates may favor the magnification of this flux.

The detection of primordial SNe will directly probe the Pop III IMF for the first time and reveal the en-

vironments in which they form. Their event rates will also trace the evolution of the first stellar populations. Pop III PI SN explosions at  $z \sim 10 - 15$  will mark the positions of primeval galaxies on the sky which might not otherwise be found by *JWST* or *TMT* (Greif et al. 2008, 2010; Wise et al. 2012). Their discovery will open our first direct window on the era of first light.

DJW is grateful for helpful discussions with Edo Berger, Ranga Ram Chary, Daniel Kasen, Avi Loeb, Pete Roming and the many participants at First Stars and Galaxies: Challenges for the Next Decade, held at UT Austin March 8 - 11, 2010. He also acknowledges support from the Bruce and Astrid McWilliams Center for Cosmology at Carnegie Mellon University. JLJ was supported by a LANL LDRD Director's Fellowship. MS thanks Marcia Rieke for making the NIRCcam filter curves available and was partially supported by NASA JWST grant NAG5-12458. DEH was supported from the National Science Foundation CAREER grant PHY-1151836. AH was supported by the US Department of Energy under contracts DE-FC02-01ER41176, FC02-09ER41618 (SciDAC), and DE-FG02-87ER40328. SEW was supported by the National Science Foundation grant AST-0909129 and the NASA Theory Program grant NNX09AK36G. Work at LANL was done under the auspices of the National Nuclear Security Administration of the U.S. Department of Energy at Los Alamos National Laboratory under Contract No. DE-AC52-06NA25396. All RAGE and SPECTRUM calculations were performed on Institutional Computing (IC) and Yellow network platforms at LANL (Conejo, Lobo and Yellowrail).

## REFERENCES

- Abel, T., Bryan, G. L., & Norman, M. L. 2000, *ApJ*, 540, 39  
—, 2002, *Science*, 295, 93
- Abel, T., Wise, J. H., & Bryan, G. L. 2007, *ApJ*, 659, L87
- Ahn, K., Iliiev, I. T., Shapiro, P. R., Mellema, G., Koda, J., & Mao, Y. 2012, *ApJ*, 756, L16
- Alvarez, M. A., Bromm, V., & Shapiro, P. R. 2006, *ApJ*, 639, 621
- Baraffe, I., Heger, A., & Woosley, S. E. 2001, *ApJ*, 550, 890
- Barkat, Z., Rakavy, G., & Sack, N. 1967, *Physical Review Letters*, 18, 379
- Beers, T. C. & Christlieb, N. 2005, *ARA&A*, 43, 531
- Blinnikov, S., Lundqvist, P., Bartunov, O., Nomoto, K., & Iwamoto, K. 2000, *ApJ*, 532, 1132
- Bromm, V., Coppi, P. S., & Larson, R. B. 1999, *ApJ*, 527, L5  
—, 2002, *ApJ*, 564, 23
- Bromm, V., Ferrara, A., Coppi, P. S., & Larson, R. B. 2001, *MNRAS*, 328, 969
- Caffau, E., Bonifacio, P., François, P., Spite, M., Spite, F., Zaggia, S., Ludwig, H.-G., Steffen, M., Mashonkina, L., Monaco, L., Sbordone, L., Molaro, P., Cayrel, R., Plez, B., Hill, V., Hammer, F., & Randich, S. 2012, *A&A*, 542, A51
- Cayrel, R., Depagne, E., Spite, M., Hill, V., Spite, F., François, P., Plez, B., Beers, T., Primas, F., Andersen, J., Barbuy, B., Bonifacio, P., Molaro, P., & Nordström, B. 2004, *A&A*, 416, 1117
- Chatzopoulos, E. & Wheeler, J. C. 2012, *ApJ*, 748, 42
- Chen, K.-J., Heger, A., & Almgren, A. S. 2011, *Computer Physics Communications*, 182, 254
- Chieffi, A. & Limongi, M. 2004, *ApJ*, 608, 405
- Clark, P. C., Glover, S. C. O., Smith, R. J., Greif, T. H., Klessen, R. S., & Bromm, V. 2011, *Science*, 331, 1040
- Colgate, S. A. 1974, *ApJ*, 187, 333
- Ekström, S., Meynet, G., Chiappini, C., Hirschi, R., & Maeder, A. 2008, *A&A*, 489, 685
- Ensmann, L. & Burrows, A. 1992, *ApJ*, 393, 742
- Frebel, A., Aoki, W., Christlieb, N., Ando, H., Asplund, M., Barklem, P. S., Beers, T. C., Eriksson, K., Fechner, C., Fujimoto, M. Y., Honda, S., Kajino, T., Minezaki, T., Nomoto, K., Norris, J. E., Ryan, S. G., Takada-Hidai, M., Tsangarides, S., & Yoshii, Y. 2005, *Nature*, 434, 871
- Frey, L. H., Even, W., Whalen, D. J., Fryer, C. L., Hungerford, A. L., Fontes, C. J., & Colgan, J. 2012, arXiv:1203.5832
- Frost, M. I., Surace, J., Moustakas, L. A., & Krick, J. 2009, *ApJ*, 698, L68
- Fryer, C. L., Whalen, D. J., & Frey, L. 2010, in *American Institute of Physics Conference Series*, Vol. 1294, American Institute of Physics Conference Series, ed. D. J. Whalen, V. Bromm, & N. Yoshida, 70–75
- Fumagalli, M., O’Meara, J. M., & Prochaska, J. X. 2011, *Science*, 334, 1245
- Gal-Yam, A., Mazzali, P., Ofek, E. O., Nugent, P. E., Kulkarni, S. R., Kasliwal, M. M., Quimby, R. M., Filippenko, A. V., Cenko, S. B., Chornock, R., Waldman, R., Kasen, D., Sullivan, M., Beshore, E. C., Drake, A. J., Thomas, R. C., Bloom, J. S., Poznanski, D., Miller, A. A., Foley, R. J., Silverman, J. M., Arcavi, I., Ellis, R. S., & Deng, J. 2009, *Nature*, 462, 624
- Gardner, J. P., Mather, J. C., Clampin, M., Doyon, R., Greenhouse, M. A., Hammel, H. B., Hutchings, J. B., Jakobsen, P., Lilly, S. J., Long, K. S., Lunine, J. I., McCaughrean, M. J., Mountain, M., Nella, J., Rieke, G. H., Rieke, M. J., Rix, H.-W., Smith, E. P., Sonneborn, G., Stiavelli, M., Stockman, H. S., Windhorst, R. A., & Wright, G. S. 2006, *Space Sci. Rev.*, 123, 485

- Gittings, M., Weaver, R., Clover, M., Betlach, T., Byrne, N., Coker, R., Dendy, E., Hueckstaedt, R., New, K., Oakes, W. R., Ranta, D., & Stefan, R. 2008, *Computational Science and Discovery*, 1, 015005
- Glover, S. C. O. & Brand, P. W. J. L. 2001, *MNRAS*, 321, 385
- Greif, T. H., Bromm, V., Clark, P. C., Glover, S. C. O., Smith, R. J., Klessen, R. S., Yoshida, N., & Springel, V. 2012, *MNRAS*, 424, 399
- Greif, T. H., Glover, S. C. O., Bromm, V., & Klessen, R. S. 2010, *ApJ*, 716, 510
- Greif, T. H., Johnson, J. L., Klessen, R. S., & Bromm, V. 2008, *MNRAS*, 387, 1021
- Greif, T. H., Springel, V., White, S. D. M., Glover, S. C. O., Clark, P. C., Smith, R. J., Klessen, R. S., & Bromm, V. 2011, *ApJ*, 737, 75
- Haiman, Z., Rees, M. J., & Loeb, A. 1997, *ApJ*, 476, 458
- Heger, A. & Woosley, S. E. 2002, *ApJ*, 567, 532
- Hosokawa, T., Omukai, K., Yoshida, N., & Yorke, H. W. 2011, *Science*, 334, 1250
- Hummel, J. A., Pawlik, A. H., Milosavljević, M., & Bromm, V. 2012, *ApJ*, 755, 72
- Iglesias, C. A. & Rogers, F. J. 1996, *ApJ*, 464, 943
- Joggerst, C. C., Almgren, A., Bell, J., Heger, A., Whalen, D., & Woosley, S. E. 2010, *ApJ*, 709, 11
- Joggerst, C. C. & Whalen, D. J. 2011, *ApJ*, 728, 129
- Johnson, J. L., Dalla Vecchia, C., & Khochfar, S. 2012, arXiv:1206.5824
- Johnson, J. L. & Khochfar, S. 2011, *ApJ*, 743, 126
- Karlsson, T., Johnson, J. L., & Bromm, V. 2008, *ApJ*, 679, 6
- Kasen, D., Woosley, S. E., & Heger, A. 2011, *ApJ*, 734, 102
- Kashlinsky, A., Arendt, R. G., Mather, J., & Moseley, S. H. 2005, *Nature*, 438, 45
- Katz, B., Sapir, N., & Waxman, E. 2012, *ApJ*, 747, 147
- Kitayama, T. & Yoshida, N. 2005, *ApJ*, 630, 675
- Kitayama, T., Yoshida, N., Susa, H., & Umemura, M. 2004, *ApJ*, 613, 631
- Komatsu, E., Smith, K. M., Dunkley, J., Bennett, C. L., Gold, B., Hinshaw, G., Jarosik, N., Larson, D., Nolte, M. R., Page, L., Spergel, D. N., Halpern, M., Hill, R. S., Kogut, A., Limon, M., Meyer, S. S., Odegard, N., Tucker, G. S., Weiland, J. L., Wollack, E., & Wright, E. L. 2011, *ApJS*, 192, 18
- Krtićka, J. & Kubát, J. 2006, *A&A*, 446, 1039
- Kudritzki, R. 2000, in *The First Stars*, ed. A. Weiss, T. G. Abel, & V. Hill, 127–+
- Lai, D. K., Bolte, M., Johnson, J. A., Lucatello, S., Heger, A., & Woosley, S. E. 2008, *ApJ*, 681, 1524
- Machacek, M. E., Bryan, G. L., & Abel, T. 2001, *ApJ*, 548, 509
- MacIntyre, M. A., Santoro, F., & Thomas, P. A. 2006, *MNRAS*, 368, 1301
- Mackey, J., Bromm, V., & Hernquist, L. 2003, *ApJ*, 586, 1
- Madau, P. 1995, *ApJ*, 441, 18
- Magee, N. H., Abdallah, Jr., J., Clark, R. E. H., Cohen, J. S., Collins, L. A., Csanak, G., Fontes, C. J., Gauger, A., Keady, J. J., Kilcrease, D. P., & Merts, A. L. 1995, in *Astronomical Society of the Pacific Conference Series*, Vol. 78, *Astrophysical Applications of Powerful New Databases*, ed. S. J. Adelman & W. L. Wiese, 51
- Maio, U., Khochfar, S., Johnson, J. L., & Ciardi, B. 2011, *MNRAS*, 414, 1145
- Matzner, C. D. & McKee, C. F. 1999, *ApJ*, 510, 379
- McKee, C. F. & Tan, J. C. 2008, *ApJ*, 681, 771
- Meiksin, A. & Whalen, D. J. 2012, arXiv:1209.1915
- Mesinger, A., Johnson, B. D., & Haiman, Z. 2006, *ApJ*, 637, 80
- Meynet, G., Maeder, A., Schaller, G., Schaerer, D., & Charbonnel, C. 1994, *A&AS*, 103, 97
- Moriya, T., Yoshida, N., Tominaga, N., Blinnikov, S. I., Maeda, K., Tanaka, M., & Nomoto, K. 2010, in *American Institute of Physics Conference Series*, Vol. 1294, *American Institute of Physics Conference Series*, ed. D. J. Whalen, V. Bromm, & N. Yoshida, 268–269
- Moriya, T. J., Blinnikov, S. I., Tominaga, N., Yoshida, N., Tanaka, M., Maeda, K., & Nomoto, K. 2012, arXiv:1204.6109
- Nakamura, F. & Umemura, M. 2001, *ApJ*, 548, 19
- Nakar, E. & Sari, R. 2010, *ApJ*, 725, 904
- Oh, S. P., Cooray, A., & Kamionkowski, M. 2003, *MNRAS*, 342, L20
- Omukai, K. & Palla, F. 2001, *ApJ*, 561, L55
- 2003, *ApJ*, 589, 677
- O’Shea, B. W. & Norman, M. L. 2007, *ApJ*, 654, 66
- 2008, *ApJ*, 673, 14
- Pan, T., Kasen, D., & Loeb, A. 2012a, *MNRAS*, 422, 2701
- Pan, T., Loeb, A., & Kasen, D. 2012b, *MNRAS*, 423, 2203
- Piro, A. L., Chang, P., & Weinberg, N. N. 2010, *ApJ*, 708, 598
- Rakavy, G. & Shaviv, G. 1967, *ApJ*, 148, 803
- Ren, J., Christlieb, N., & Zhao, G. 2012, arXiv:1207.4536
- Rogers, F. J., Swenson, F. J., & Iglesias, C. A. 1996, *ApJ*, 456, 902
- Rydberg, C.-E., Zackrisson, E., Lundqvist, P., & Scott, P. 2012, arXiv:1206.0007
- Rydberg, C. E., Zackrisson, E., & Scott, P. 2010, in *Cosmic Radiation Fields: Sources in the early Universe (CRF 2010)*, ed. M. Raue, T. Kneiske, D. Horns, D. Elsaesser, & P. Hauschildt, 26
- Scannapieco, E., Madau, P., Woosley, S., Heger, A., & Ferrara, A. 2005, *ApJ*, 633, 1031
- Schaerer, D. 2002, *A&A*, 382, 28
- Smith, B. D. & Sigurdsson, S. 2007, *ApJ*, 661, L5
- Smith, B. D., Turk, M. J., Sigurdsson, S., O’Shea, B. W., & Norman, M. L. 2009, *ApJ*, 691, 441
- Smith, N. & McCray, R. 2007, *ApJ*, 671, L17
- Stacy, A., Greif, T. H., & Bromm, V. 2010, *MNRAS*, 403, 45
- 2012, *MNRAS*, 422, 290
- Su, J., Stiavelli, M., Oesch, P., Trenti, M., Bergeron, E., Bradley, L., Carollo, M., Dahlen, T., Ferguson, H. C., Giavalisco, M., Koekemoer, A., Lilly, S., Lucas, R. A., Mobasher, B., Panagia, N., & Pavlovsky, C. 2011, *ApJ*, 738, 123
- Tan, J. C. & McKee, C. F. 2004, *ApJ*, 603, 383
- Tanaka, M., Moriya, T. J., Yoshida, N., & Nomoto, K. 2012, *MNRAS*, 422, 2675
- Tolstov, A. G. 2010, *Astronomy Letters*, 36, 109
- Tominaga, N., Blinnikov, S., Baklanov, P., Morokuma, T., Nomoto, K., & Suzuki, T. 2009, *ApJ*, 705, L10
- Tornatore, L., Ferrara, A., & Schneider, R. 2007, *MNRAS*, 382, 945
- Trenti, M. & Stiavelli, M. 2009, *ApJ*, 694, 879
- Trenti, M., Stiavelli, M., & Michael Shull, J. 2009, *ApJ*, 700, 1672
- Turk, M. J., Abel, T., & O’Shea, B. 2009, *Science*, 325, 601
- van Marle, A. J., Smith, N., Owocki, S. P., & van Veelen, B. 2010, *MNRAS*, 407, 2305
- Vink, J. S., de Koter, A., & Lamers, H. J. G. L. M. 2001, *A&A*, 369, 574
- Weaver, T. A., Zimmerman, G. B., & Woosley, S. E. 1978, *ApJ*, 225, 1021
- Weinmann, S. M. & Lilly, S. J. 2005, *ApJ*, 624, 526
- Whalen, D., Abel, T., & Norman, M. L. 2004, *ApJ*, 610, 14
- Whalen, D., Hueckstaedt, R. M., & McConkie, T. O. 2010, *ApJ*, 712, 101
- Whalen, D. & Norman, M. L. 2006, *ApJS*, 162, 281
- 2008a, *ApJ*, 673, 664
- Whalen, D., O’Shea, B. W., Smidt, J., & Norman, M. L. 2008a, *ApJ*, 679, 925
- Whalen, D., van Veelen, B., O’Shea, B. W., & Norman, M. L. 2008b, *ApJ*, 682, 49
- Whalen, D. J., Even, W., Lovekin, C. C., Fryer, C. L., Holz, D. H., Stiavelli, M., & Knight, C. 2012a, *ApJ*, submitted
- Whalen, D. J. & Fryer, C. L. 2012, *ApJ*, 756, L19
- Whalen, D. J., Fryer, C. L., Holz, D. E., Heger, A., Woosley, S. E., Stiavelli, M., Even, W., & Frey, L. L. 2012b, arXiv:1209.3457
- Whalen, D. J., Joggerst, C. C., Fryer, C. L., Stiavelli, M., Heger, A., & Holz, D. E. 2012c, arXiv:1209.5459
- Whalen, D. J. & Norman, M. L. 2008b, *ApJ*, 672, 287
- Wise, J. H. & Abel, T. 2005, *ApJ*, 629, 615
- 2008a, *ApJ*, 684, 1
- 2008b, *ApJ*, 685, 40
- Wise, J. H., Turk, M. J., Norman, M. L., & Abel, T. 2012, *ApJ*, 745, 50
- Woosley, S. E. & Heger, A. 2007, *Phys. Rep.*, 442, 269
- Woosley, S. E., Heger, A., & Weaver, T. A. 2002, *Reviews of Modern Physics*, 74, 1015
- Yoshida, N., Omukai, K., & Hernquist, L. 2008, *Science*, 321, 669